

Improving Fatigue Performance of Spot Welds in Advanced High-Strength Steels

Identification of microstructural enablers and an optimization strategy for the spot welding process were developed to improve fatigue performance of spot welds in advanced high-strength steels

BY S. K. VANIMISETTI AND D. R. SIGLER

ABSTRACT

Significant variations in fatigue performance of spot welded advanced high-strength steels suggest that improvements may be achieved through optimization of the spot welding process. Microstructural analyses performed on fatigue tested welds found that fatigue life correlates well with the location and orientation of the fine-grained heat-affected zone (FGHAZ). In welds with high FGHAZ angles, the fatigue crack is deflected either toward the sheet surface along the FGHAZ or into the harder coarse-grained HAZ and nugget, where crack growth is either retarded or arrested. Modeling confirmed that stress intensity at the tip of the fatigue crack is lower for steeper crack orientations, which slows crack growth and improves fatigue life. A “virtual” optimization methodology employing design of experiments was developed to tailor the weld microstructure for improved fatigue life. The modified welding process demonstrated steeper FGHAZ angles, which should significantly improve the fatigue life of the spot weld.

Signers use increased sheet thickness, which counters the intent of the use of AHSS for lightweighting. The observed variation in high cycle fatigue life could not be attributed to the presence or absence of weld surface cracks, faying interface cracks, or expulsion events (Ref. 3).

A recent experimental study that restricted attention to welding cycle parameters has shown that significant improvement in fatigue strength can be obtained by changing the weld schedule (Ref. 4). An integrated computational modeling technique, which incorporated the microstructural zone and residual stress information from the resistance welding simulation into the mechanical model, has also been used to understand the effect of the spot welding process on the performance of the weld (Ref. 5). However, both these studies did not carry out a systematic investigation to identify the process parameters that affect the distribution of weld microstructural zones that in turn affect its mechanical performance, especially in fatigue.

Microstructural Aspects of Fatigue Failure

A schematic of the common lap shear configuration of a spot weld joint is shown in Fig. 1 along with the weld microstructural zones in the cross-section A-A that is aligned with the loading axis. The microstructure and hardness of significant weld regions in spot welds of AHSS, such as DP600, have been widely investigated (Refs. 6, 7). These regions include the base material, transformed fine-grained heat-affected zone (FGHAZ), transformed coarse-grained heat-affected zone (CGHAZ), and weld nugget. A micrograph demarcating these weld microstructural regions in the cross-section A-A of a DP600 AHSS spot weld is shown in Fig. 1. The hardness in the microstructural zones increases moving from the base material (HV 225) across the FGHAZ (HV 358) and into the CGHAZ and weld nugget (HV for both ~430). Investigations of fatigue failure in lap-shear spot welds of

Introduction

Advanced high-strength steels (AHSS) are used extensively within the automotive industry for structural applications. The primary reasons for selecting AHSS materials are to reduce vehicle weight and to improve energy management during a crash event. Advanced high-strength steels such as the dual-phase (DP) and the transformation induced plasticity (TRIP) steels have good formability and crash-worthiness characteristics because of the combination of high strength and ductility. Integration of AHSS materials in the body-in-white structure presents challenges related to joining. Resistance spot welding is the primary joining process for the automotive body structure due to its efficiency and economic feasibility. Thus, improvements to the performance and durability, i.e., fatigue strength, of AHSS spot weld joints will improve vehicle durability.

A comprehensive database of fatigue performance of spot welded steels ranging

from interstitial-free (IF) steels to conventional advanced high-strength steels, to very high-strength boron steels was compiled (Ref. 1). The study found that spot weld fatigue behavior is controlled mainly by geometric factors such as sheet thickness and weld diameter. Despite the significant difference in tensile properties and composition between various types of steels, their spot welded joints showed very similar fatigue performance between 10,000 and 1,000,000 cycles, primarily due to recrystallization near the weld region (Refs. 1, 2). Another study found a significant statistical spread in the high cycle fatigue life observed for TRIP590 and DP600 spot-welded lap-shear joints (Ref. 3). As shown in Fig. 1, this spread is over an order of magnitude in cycles to failure at 600-lb load. This variation in high cycle fatigue life requires that de-

KEYWORDS

Resistance Spot Welding
Advanced High-Strength Steels
Microstructure
Fatigue Life
Optimization

S. K. VANIMISETTI (sampath.vanimisetti@gm.com) is with Vehicle Engineering, GM Tech Center India, Bangalore, India. D. R. SIGLER is with Manufacturing Systems Research Lab, GM R&D Center, Warren, Mich.

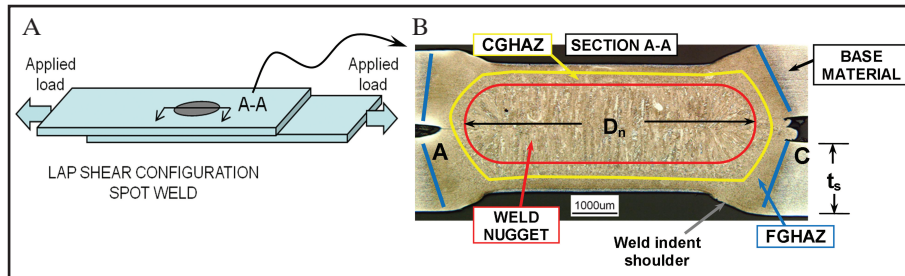


Fig. 1 — Schematics of the following: A — A lap shear spot weld joint; B — optical micrograph of section A-A along the load axis in a 1.6-mm DP600 spot weld. The labeled microstructural zones are weld nugget, coarse-grained heat-affected zone (CGHAZ), fine-grained heat-affected zone (FGHAZ), and the unaffected base material. Here, t_s is the sheet thickness and D_n is the weld nugget size.

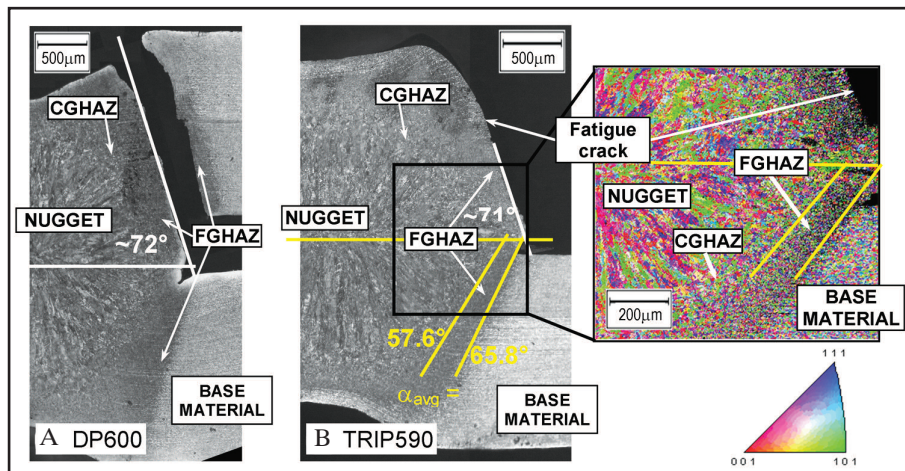


Fig. 2 — Influence of microstructural zones on the fatigue crack growth in A — DP600; B — TRIP590 spot welds.

AHSS using careful sectioning (Ref. 8) and the potential drop method (Ref. 4) have shown the existence of three stages of fatigue failure, namely, crack initiation, crack growth, and sheet failure. Fatigue crack initiation occurs at the notch root locations that are aligned with the loading axis (see points A and C in Fig. 1), and it accounts for 30–50% of the total fatigue life. The fatigue crack then propagates toward the outer sheet surface along the FGHAZ, which provides a path for easier crack growth (Refs. 4, 6, 7, 9–16).

This study was undertaken to identify significant microstructural features that govern the fatigue life of spot welds and their relation to key process parameters. Understanding this relation would facilitate the optimization of the welding process for improving the fatigue performance of spot-welded AHSS. A validated finite element

model of the spot welding process was developed using a commercial resistance spot welding tool SORPAS® (Refs. 17–19). Subsequently, this computer model was used along with a design of experiments framework in MINITAB® (Ref. 20) in order to optimize the welding process. The optimized candidate electrode designs and weld schedules were used to fabricate weld specimens for microstructural analysis to determine whether the preferred spatial distribution of the microstructure was achieved.

Experimental and Modeling Procedures

Experimental Procedure

Weld specimens and fatigue performance data from a previous study (Ref. 3) of spot-welded 1.6-mm galvannealed

TRIP590 and 1.6-mm hot dip galvanized (HDG) DP600 were chosen. The chemical compositions of the materials and the details of spot welding equipment are given in the above reference (Ref. 3). The conventional multipulse weld schedule for 1.6-mm AHSS is listed in Table 1.

Metallographic examination of weld cross-section A-A (Fig. 1) was performed using optical microscopy. An etching procedure based on recommendations for low-alloy steels (Ref. 21) was used to reveal the microstructure. Microstructural parameters such as the nugget size, HAZ width, and FGHAZ orientation were measured from a high-resolution image of the microstructure using image analysis software, ImagePro® (Ref. 22). The procedure used to determine orientation of the FGHAZ is illustrated in Fig. 2. The angles between the extreme boundaries of the FGHAZ (inclined yellow lines), i.e., the CGHAZ-FGHAZ and FGHAZ-base material transition regions, and the faying interface (horizontal yellow line) are measured. The FGHAZ angle is defined as the average of these two measurements. This measurement method uses the inclination of well-defined FGHAZ boundaries to compute the average FGHAZ inclination, as shown in Fig. 2. Since the SORPAS® models are well calibrated and accurate, the location and inclination of the FGHAZ boundaries are consistent between experimental and simulation. For the validation exercise performed during the study, the boundary of the FGHAZ orientation in experiments and simulation was well defined and the image analysis using ImagePro gave repeatable readings.

Electron backscattered diffraction (EBSD) analysis was performed on several samples. Sample surfaces were prepared by mechanical polishing followed by electropolishing. Inverse pole figure (IPF) maps were generated from the EBSD analysis. The EBSD scanning was conducted at a step size of 0.2 μm or lower using a field emission Zeiss scanning electron microscope with an HKL camera. The grain boundaries were identified with > 5-deg misorientation. The IPF maps were used to generate maps of grain morphology in the vicinity of the notch root.

Table 1 — Conventional Welding Process Parameters*

Electrode Design	Weld Force (kN)	Weld Time (ms)	Weld Current (kA)	Cool Time (ms)	Pulses (no.)	Hold Time (ms)
MWZ-6006: 4.8-mm FD, flat FR	4.2	130	7 to 11	40	3	1000

* Coolant water flow rate was 1.0 gal/min at a nominal temperature of 23°C. Electrodes were made of Cu-Zr, C15000 alloy. Legend: FD – face diameter, FR – face radius of curvature.

Finite Element Modeling Procedure

Modeling of Spot Weld Fatigue Failure

In order to assess the fatigue performance of the weld, the stress intensity factors and the crack propagation rates at the spot weld notch root have to be estimated. There are many theoretical approaches to estimate stress intensities at the notch root (Refs. 12, 23–25). However, theoretical methods do not account for aspects such as weld indentation, process-induced weld cracks, and crack growth. Recently, Wang et al. (Ref. 26) utilized computational methods such as finite element (FE) modeling to study the fracture mechanics of spot welds accounting for kinked crack morphologies, i.e., notch root with existing process-induced weld crack. The FE modeling method can also account for details such as weld indentation, crack growth, and notch root radius. In this study, the approach presented in Ref. 26 is adapted to study the change in stress intensity factor at the tip of a finitely long fatigue crack emanating from the notch root. Such a method allows tracking of the stress intensities as the crack propagates along various paths inclined with the faying interface. A finite element (FE) model of the tensile lap-shear spot weld based on Ref. 26 was developed to estimate the stress intensity factors at the tip of a fatigue crack growing from the notch root, inclined at various angles with respect to the faying interface. The modeling method, boundary conditions, and loading are as described for lap-shear specimens in Ref. 26. A more detailed description of the modeling method is beyond the scope of this study and can be found elsewhere (Ref. 27). The symmetric half of a spot welded stack was modeled by considering design parameters such as sheet thickness, nugget size, and electrode indentation depth. The solid model was then discretized using a combination of 20-noded 3D isoparametric brick elements with full and reduced order integration. Boundary and contact conditions replicating the lap-shear test were imposed on the FE mesh. A special focused mesh at the notch root and the tip of the fatigue crack was used to estimate the stress intensity factors, K_I , K_{II} , and K_{III} using the interaction integral and the domain integral method available in Abaqus®/Standard (Ref. 28).

Modeling of Resistance Spot Welding

The computer simulation of the resistance spot welding process was carried out using commercial software SORPAS® (Ref. 17). It utilizes the finite element technique to solve a sequentially coupled, transient electrical-thermal-mechanical multiphysics model. Input data to the simulation include parameters such as weld

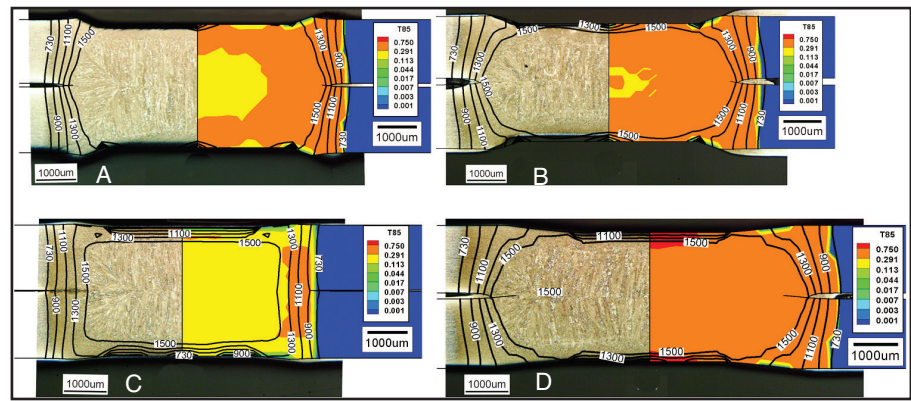


Fig. 3 — Comparison of weld microstructure observed from the experiments and those predicted from SORPAS® simulations using peak temperature and cooling rate distribution for the following: A — MWZ-6006 electrode, single-pulse, 200-ms 11-kA schedule; B — MWZ-6006 electrode, 3-pulse, 130-ms 9-kA schedule; C — 25-mm radiused electrode, single-pulse, 200-ms 9-kA schedule; D — 25-mm radiused electrode, 3-pulse, 130-ms 11-kA schedule.

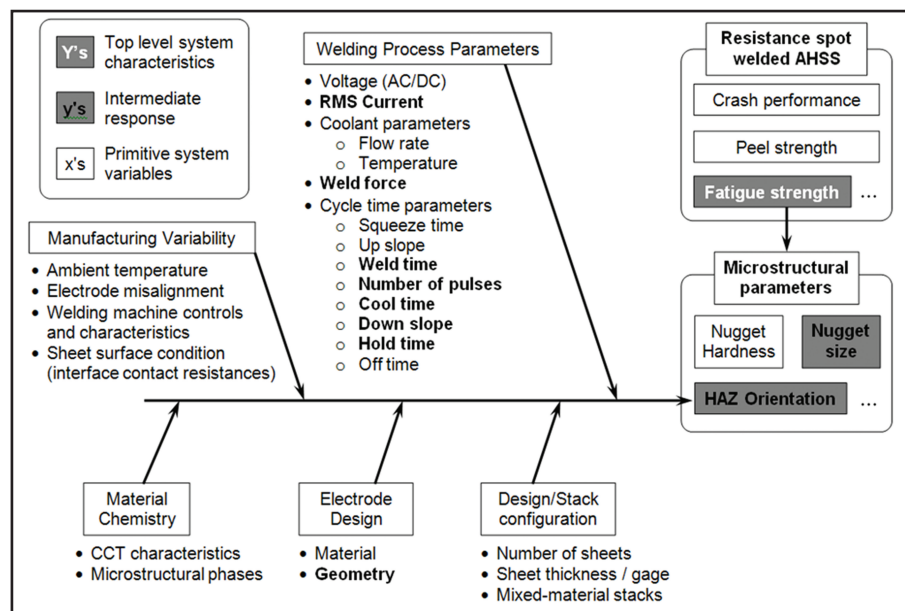


Fig. 4 — Schematic depicting the cause-and-effect relationship between the fatigue performance of the spot weld and key welding process variables that affect the local distribution of the weld microstructure.

force, current waveform, weld time, pulsations; electrode geometry and cooling; along with sheet gauges, alloys, coatings, and stack configuration. The software can also incorporate user-specified electrode designs in the simulations. The temperature-dependent electrical, mechanical, and metallurgical properties of various sheet, coating, and electrode materials

along with calibrated values for the electrode/sheet and sheet/sheet contact-interface resistances are available in the built-in database. In the simulations, the off and idle times were kept long enough to attain thermal and phase-transformation equilibrium for accurate prediction of the microstructural zones.

The spot welding process is simulated

Table 2 — Microstructural Zones in Steel Welds and Associated Peak Temperature Ranges (Ref. 24)

Microstructural Zones	Peak Temperature Range (°C)
Fusion zone	$T_{pk} > T_m$ (1550)
Coarse-grain HAZ	$1100 < T_{pk} < 1300$
Fine-grain HAZ (austenite)	$Ac3(900) < T_{pk} < 1100$
Intercritical HAZ (partial austenite)	$Ac1(730) < T_{pk} < Ac3(900)$
Tempered region	$T_{pk} < Ac1(730)$

WELDING RESEARCH

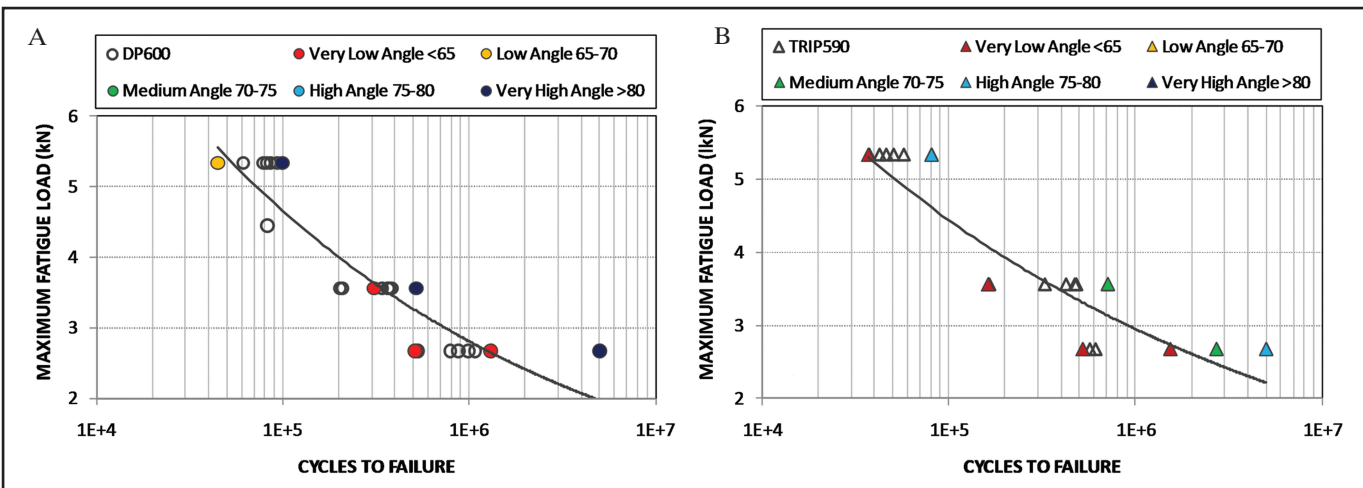


Fig. 5 — Influence of FGHAZ angle on the fatigue performance of A — DP600; B — TRIP590 spot welds.

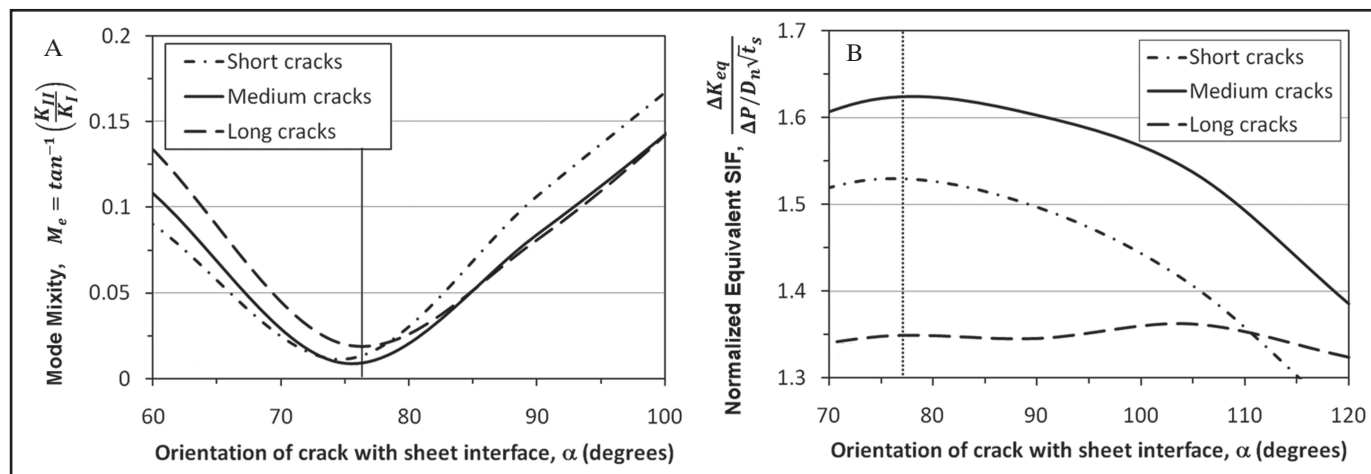


Fig. 6 — Effect of fatigue crack orientation on A — Mode mixity M_e ; B — equivalent stress intensity factor K_{eq}

over an idealized axisymmetric section of the electrode-sheet stack, which is discretized using 4-noded finite elements, and appropriate electrical, thermal, and mechanical boundary conditions are applied. Details of the finite element mesh, domain settings, and boundary conditions for the model can be found elsewhere (Ref. 17). The finite element model available in SORPAS® has been successfully applied to study the resistance spot welding of steels, including AHSS (Refs. 18, 19). The studies have shown that the software is able to accurately determine the variation in temperature within the weld.

In this work, the spatial and temporal variations of temperature fields obtained from the SORPAS® finite element model were postprocessed using an external algorithm to determine the spatial distribution of various weld microstructural zones.

Identification of Weld Microstructural Zones from Simulations

The spatial maps of peak temperature (T_{pk}) and T85 cooling rate, i.e., the time taken for the sheet material to cool between 800° and 500°C during the welding process, were obtained from the simula-

tions. Since the cooling rates experienced during the spot welding process are as high as 6000°C/s for 1.6-mm DP600 sheet material (Refs. 6, 19), only T_{pk} is sufficient to determine the local microstructural phase as determined by the CCT diagrams for the sheet material (Ref. 29). A macro-enabled visualization software, TEC-PLOT® (Ref. 30), was used to process the spatial maps of T_{pk} and T85 cooling rates to generate a grayscale contour image with levels demarcated by the peak temperature listed in Table 2. This grayscale image was processed by an image analysis software, ImagePro® (Ref. 22), which isolated

Table 3 — Welding Process Parameters* Used for the Validation Study

Electrode Design	Weld Force (kN)	Weld Time (ms)	Weld Current (kA)	Cool Time (ms)	Pulses (no.)	Hold Time (ms)
MWZ-6006: 4.8-mm FD, flat FR	4.2	200	7 to 11	—	1	1000
MWZ-6006: 4.8-mm FD, flat FR	4.2	130	8 to 11	40	3	1000
Radius: 12-mm FD, 25-mm FR	4.2	200	7 to 11	—	1	1000
Radius: 12-mm FD, 25-mm FR	4.2	130	8 to 11	40	3	1000

* Coolant water flow rate was 1.0 gal/min at a nominal temperature of 23°C. Electrodes were fabricated from Cu-Zr, C15000 alloy. Legend: FD – face diameter, FR – face radius of curvature.

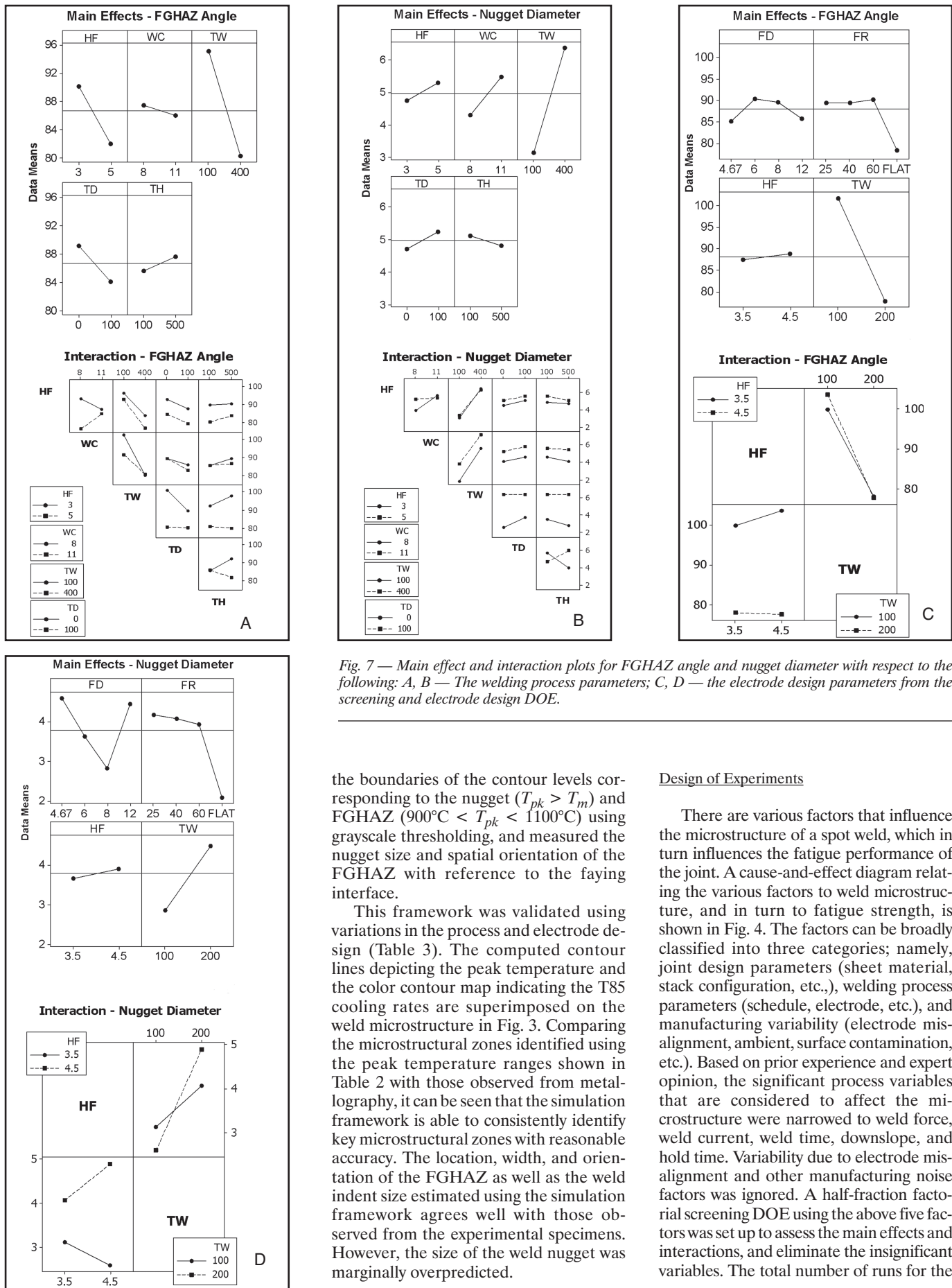


Fig. 7 — Main effect and interaction plots for FGHAZ angle and nugget diameter with respect to the following: A, B — The welding process parameters; C, D — the electrode design parameters from the screening and electrode design DOE.

the boundaries of the contour levels corresponding to the nugget ($T_{pk} > T_m$) and FGHAZ ($900^\circ\text{C} < T_{pk} < 1100^\circ\text{C}$) using grayscale thresholding, and measured the nugget size and spatial orientation of the FGHAZ with reference to the faying interface.

This framework was validated using variations in the process and electrode design (Table 3). The computed contour lines depicting the peak temperature and the color contour map indicating the T85 cooling rates are superimposed on the weld microstructure in Fig. 3. Comparing the microstructural zones identified using the peak temperature ranges shown in Table 2 with those observed from metallography, it can be seen that the simulation framework is able to consistently identify key microstructural zones with reasonable accuracy. The location, width, and orientation of the FGHAZ as well as the weld indent size estimated using the simulation framework agrees well with those observed from the experimental specimens. However, the size of the weld nugget was marginally overpredicted.

Design of Experiments

There are various factors that influence the microstructure of a spot weld, which in turn influences the fatigue performance of the joint. A cause-and-effect diagram relating the various factors to weld microstructure, and in turn to fatigue strength, is shown in Fig. 4. The factors can be broadly classified into three categories; namely, joint design parameters (sheet material, stack configuration, etc.), welding process parameters (schedule, electrode, etc.), and manufacturing variability (electrode misalignment, ambient, surface contamination, etc.). Based on prior experience and expert opinion, the significant process variables that are considered to affect the microstructure were narrowed to weld force, weld current, weld time, downslope, and hold time. Variability due to electrode misalignment and other manufacturing noise factors was ignored. A half-fraction factorial screening DOE using the above five factors was set up to assess the main effects and interactions, and eliminate the insignificant variables. The total number of runs for the

WELDING RESEARCH

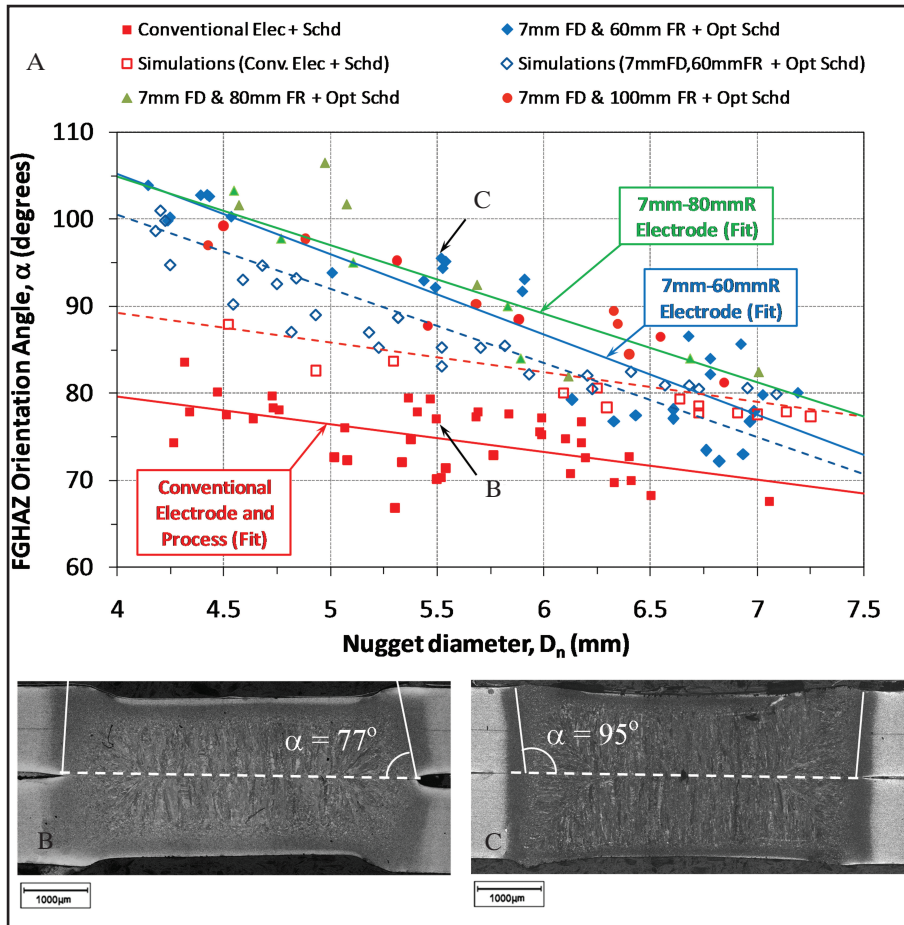


Fig. 8—A—A map of nugget diameter and FGHAZ orientation showing data from simulation and microstructures of test welds. Microstructures of welds with a nominal nugget diameter of 5.5 mm for B—conventional electrode and multipulse schedule and C—optimized electrode and weld schedule, showing improvements in FGHAZ angle.

screening DOE was 16. Main process variables identified from the screening DOE were combined with electrode geometry variables, namely, face diameter and face radius of curvature to perform an electrode design optimization DOE to maximize FGHAZ angle for a target range of 5–6 mm nugget size. This DOE was set up using a Taguchi Orthogonal Array Design (L₁₆ - 4^{**2} 2^{**2}) with 4 factors and a total of 16

runs. A summary of the factor levels for these two DOEs is presented in Table 4.

Results and Discussion

Spot Weld Microstructure and Fatigue Failure

Tested fatigue samples from a previous study (Ref. 3) on spot welded lap-shear

joints of 1.6-mm-thick DP600 and TRIP590 sheet materials were taken and cross-sectioned for metallographic examination. Figure 2 shows sections for DP600 and TRIP590 welds that failed in high cycle fatigue at a 600-lb load. The fatigue crack has clearly grown from the faying interface through the FGHAZ to the outer surface of the sheet resulting in failure. An IPF map was generated from an EBSD analysis of the TRIP590 sample (see inset in Fig. 2B) in order to verify the observation from optical micrographs. The size and orientation of the grains can be assessed using the IPF map color legend, shown under the inset in Fig. 2B. Both optical micrographs and IPF maps consistently identified the spatial variation in the grain structure from the base material to the nugget. The high cycle fatigue failure is contained within the fine grain structure in the FGHAZ region for a significant portion of the crack growth stage.

A cursory examination of the microstructures suggested that a correlation might exist between FGHAZ orientation and fatigue life. To verify this, more detailed measurements of the FGHAZ were carried out on all selected weld sections from the previous study (Ref. 3). Both the DP600 and TRIP590 materials tested at high load (1200 lb) and at low load (600 lb) indicated that samples with the lower FGHAZ angle of ~60 deg had shorter life, by almost an order of magnitude compared to samples with a higher FGHAZ angle of ~80 deg. This observation seems to explain the variation in fatigue performance of spot welded joints, which could not be attributed to either expulsion or weld surface cracks based on previous investigation (Ref. 3).

Interestingly, the measurements also revealed that the FGHAZ angle in the galvanized DP600 material was consistently higher by ~8 deg than that in the galvannealed TRIP590 material. The reason for this difference could be due to the coatings on the sheet surface, the bulk resistance of the steel, or a combination of the two. The galvannealed TRIP590 material has a higher surface resistance due to the

Table 4—Welding Process and Radiused Electrode Design Parameters* for the DOE Studies

Screening DOE				Electrode Design DOE			
Hold Time (TH) ms	Weld Current (WC) kA	Downslope Time (TD) ms	Hold Force (HF) kN	Weld Time (TW) kA	Face Diameter (FD) mm	Face Radius of Curvature (FR) mm	
100–500	8–11	0–100	3–5	100–500	4.8, 7	Flat, 60, 80, 100	

* Coolant water flow rate was 1.0 gal/min at a nominal temperature of 23°C. Electrodes were fabricated from Cu-Zr, C15000 alloy. For screening DOE, the electrode design parameters FD and FR were 6 and 40 mm, respectively. For electrode design DOE, parameters TH, WC, and TD were set at 500 ms, 10 kA, and 0 ms, respectively. Note: HF and TW are common parameters between the two DOEs.

Table 5 — Welding Process Parameters* for the Test Welds

Electrode Design	Weld Force (kN)	Weld Time (ms)	Weld Current (kA)	Cool Time (ms)	Pulses (no.)	Hold Time (ms)
Radius: 7-mm FD, 60, 80, and 100 mm FR	3.0	100–400	11	—	1	1000

* Coolant water flow rate was 1.0 gal/min at a nominal temperature of 23°C. Electrodes were made of Cu-Zr, C15000 alloy. Legend: FD – face diameter, FR – face radius of curvature.

applied Zn-Fe coating and higher bulk electrical resistance as well as decreased thermal conductivity due to the richer chemistry, which result in higher levels of heat produced at the faying interface than for the galvanized DP600 material, thereby accelerating nugget formation and lateral growth at that interface. Rapid lateral growth of the nugget at the faying interface would tend to reduce the FGHAZ angle. In contrast, the presence of a galvanized coating on the DP600 material would result in reduced contact resistance at all interfaces as the Zn coating melts. Heating through the bulk material would play a more important role, which would create a more uniform heat profile through the sheet material and tend to result in a more vertical FGHAZ angle.

The profound effect of FGHAZ angle on fatigue life becomes apparent by plotting FGHAZ angle against cycles to failure as shown in Fig. 5. Samples with FGHAZ angle measurements are indicated by filled symbols, whereas those without are shown using hollow symbols. The FGHAZ angles were segregated into five distinct ranges, namely, very low angles (<65 deg), low angles (65–70 deg), medium angles (70–75 deg), high angles (75–80 deg), and very high angles (>80 deg). It is apparent from Fig. 5A, B that the FGHAZ angle correlates directly with fatigue life at all load levels, i.e., higher FGHAZ angles correlate with extended life. This effect is more pronounced for high cycle fatigue at 600-lb load, which shows almost an order of magnitude increase in the fatigue life as the FGHAZ orientation increases from low to high angles.

Influence of FGHAZ Orientation on High Cycle Fatigue Crack Propagation

As noted previously, fatigue crack growth usually occurs along the FGHAZ, which provides a path for easier crack growth. Fatigue crack propagation usually occurs along the FGHAZ at an angle of about 74 deg with reference to the faying interface (Ref. 13). A similar angle of about 72 deg (see measurement shown in white color in Fig. 2) was observed in this study. To better understand the relationship between FGHAZ angle and fatigue failure, finite element analyses were carried out to determine the stress intensity

factors (SIFs) at the tip of fatigue cracks for cracks of various length orientated at angle ‘ α ’ with respect to the faying interface. The short, medium, and long crack lengths considered in the finite element study are 1, 5, and 10% of the sheet thickness, respectively. The critical fatigue crack initiation and growth from points A and C along the loading symmetry plane (section A-A in Fig. 1) occurs predominantly under mixed-mode I and II loading as the mode-III component vanishes to zero on the symmetry plane. The mode-I and mode-II SIFs (K_I and K_{II}) at the crack tip were estimated using the finite element simulations described in the previous sections. The equivalent SIF (K_{eq}) was estimated using the following equation (Refs. 31–33, 36),

$$K_{eq} = \sqrt{K_I^2 + \beta K_{II}^2} \quad (1)$$

In Equation 1, β is a material parameter. Its value is often close to 1.0. The fatigue crack initiation occurs in the direction (θ_o) that satisfies the MTS-criterion (Refs. 31–35). It can be written in terms of the mode-mixity ($M_e = 2/\pi \tan^{-1}\{K_{II}/K_I\}$) (Ref. 32) prevailing at the crack tip as

$$\theta_o = \cos^{-1} \left[\frac{3\sin^2\left(\frac{\pi M_e}{2}\right) \pm \sqrt{\cos^4\left(\frac{\pi M_e}{2}\right)}}{+8\cos^2\left(\frac{\pi M_e}{2}\right)\sin^2\left(\frac{\pi M_e}{2}\right)} \right] / \left[\frac{\cos^2\left(\frac{\pi M_e}{2}\right) + 9\sin^2\left(\frac{\pi M_e}{2}\right)}{\cos^2\left(\frac{\pi M_e}{2}\right)} \right] \quad (2)$$

The mode-mixity M_e varies between 0 for pure mode-I opening and 1 for mode-II sliding. Under linear elastic conditions and mixed mode-I and II loading at the crack tip, which is representative of the critical crack growth at the symmetry plane during high cycle fatigue of lap-shear specimens, the energy release rate (J) can be directly proportional to K_{eq}^2 (Refs. 34, 35). From Equation 2, it can be seen that $\theta_o \sim 0$ deg for $M_e \rightarrow 0$, i.e., the crack will initiate and continue to grow in the direction where M_e is minimized. Therefore, the fatigue crack is most likely to propagate in the direction that minimizes M_e (MTS-criterion) and maximizes K_{eq} (J-criterion).

The results of the finite element modeling study are presented in Fig. 6, which shows the mode-mixity (M_e) and cyclic equivalent stress intensity factor ($K_{eq} = (1-R) K_{eq}^{max}$, R is the fatigue load ratio) computed from the finite element simulations for various crack orientation angles α . For all three crack lengths, M_e is minimized and ΔK_{eq} is maximized at a crack orientation of ~76 deg. Therefore, the preferred direction of fatigue crack propagation in lap-shear joints is ~76 deg. This conclusion supports the experimental observations, which indicate that samples with average FGHAZ angles around the preferred angle of ~76 deg for crack growth, produced cracks that grew at angles close to the preferred angle, while being contained within the FGHAZ. In contrast, for welds with medium to high FGHAZ angles that result in extended fatigue life, the cracks propagated along the FGHAZ or deflected into the nugget. It can be argued that this apparent improvement in fatigue life is due to the increase in the life spent in crack propagation (N_p) along the FGHAZ (Refs. 31, 33, 36),

$$N_p = \int_{a_i}^{a_f} \frac{t_s}{C((1-R)K_{eq}^{max})^m \sin(\theta_o)} \quad (3)$$

In Equation 3, t_s is the sheet thickness, coefficient C and exponent m are parameters defining the material in which the fatigue crack is propagating, and R is the fatigue load ratio. From Equation 3, it is evident that the cycles spent in propagating the fatigue crack across the sheet thickness can be increased by reducing either the equivalent stress intensity factor (K_{eq}) or the material constants (C and m). From Fig. 6B, it can be seen that fatigue cracks that propagate along FGHAZ oriented at angles higher than ~76 deg experience lower K_{eq} . Further, if the crack is not deflected along the FGHAZ, it encounters the hard martensitic nugget, which has significantly lower exponent ($m \approx 2.25$) compared to the FGHAZ or base materials ($m \approx 3.0$) (Ref. 37). In any of the above circumstances, the crack growth rates are expected to be reduced, which increases the cycles spent propagating the fatigue crack.

Interestingly, microstructural analyses of the DP600 and TRIP590 welds, which were produced using a variety of single pulse and multipulse weld schedules along

with a standard ball-nose electrode design, revealed that a majority of the welds contained FGHAZ regions oriented close to 76 deg to the faying interface. This orientation of the FGHAZ is favorably aligned for high crack growth rates and provides a path of least resistance. Based on the discussion presented previously, it appears that the fatigue life of spot weld joints in AHSS might be improved by optimizing the process to achieve FGHAZ angles in the range of 80 and 120 deg. The optimization framework described previously is now used to identify the weld process and electrode design parameter values that will enable the process to achieve these FGHAZ angles.

Weld Process Modeling and Design of Experiments

Screening DOE

A preliminary screening DOE was run to investigate responses for FGHAZ orientation and weld nugget diameter, based on variables of weld force (HF), hold time (TH), weld current (WC), weld time (TW), and downslope (TD). The levels corresponding to these factors are listed in Table 4. The main effects and interaction plots for FGHAZ orientation and nugget diameter are shown in Fig. 7A and B, respectively. Figure 7A clearly indicates that weld force and weld time are two major process parameters that significantly affect the FGHAZ angle, i.e., short time and low force increase the FGHAZ angle. Interactions were observed between hold force (HF) and weld current (WC) as well as downslope (TD) and hold time (TH). The interaction between hold force and weld current is expected as the total heat input into the sheet metal, which determines the shape and size of the weld nugget is dependent on the two weld parameters. It is interesting to note from Fig. 7B that while the nugget size is significantly affected by the same parameters as FGHAZ orientation, i.e., weld time and weld force, the trends are reversed. It is therefore essential to identify the optimal process window to mitigate this trade-off and maximize the FGHAZ angle for the target nugget size.

Electrode Weld Face Effects

The results of the screening DOE showed that low weld force promotes higher FGHAZ angles. This observation suggests that the nature of mechanical contact at the electrode/sheet interface can be suitably modified to affect the spatial distribution of the FGHAZ. It is argued that electrode design parameters such as face radius of curvature and lateral diameter, which have a strong influence

on the area or width of mechanical contact, can be optimized to extend the HAZ near the outer surface compared to that at the faying interface. This is likely to result in a high orientation angle for the FGHAZ. Conventional electrodes for welding steel are typically domed electrodes that often have a weld face several mm in diameter, either flat or gently radiused, that contacts the sheet material. In the remainder of this paper, electrodes that have a weld face with a radius for contacting the sheet material are termed "radiused electrodes." To understand the effect of the above electrode design parameters on the FGHAZ orientation, the contact size, electrical resistance, and heat input at the electrode/sheet interface are estimated. Since constant current is imposed during the welding process, the total heat input across the electrode/sheet interface is a function of the interface resistance. The total heat input (Q_{E-S}) due to effective resistance (Ω_{E-S}) at the interface can be represented using an equivalent parallel circuit consisting of infinitesimal interface elements, whose resistance is inversely proportional to the local contact pressure or normal stress σ_n acting on the interface (Ref. 17).

$$Q_{E-S} = I^2 \Omega_{E-S} = \frac{\Psi t_i I^2 t_{weld}}{\int \sigma_n(r) 2\pi r dr} \quad (4)$$

In Equation 4, I is the current, t_{weld} is the weld time, a is the contact radius, and t_i is the thickness of the contact interface. Ψ is a factor combining mechanical and electrical properties of the electrode/sheet materials as well as the surface conditions. The integral of the local normal stress in the denominator of Equation 4 is the total contact load as suggested by the Hertz contact theory (Ref. 38), i.e., $P = \int \sigma_n(r) 2r dr$. Therefore, for a given combination of materials and processing conditions (constant weld force, P) the total heat input at the interface is the same for any radius of the electrode face. However, the interface contact radius a increases with the electrode face radius when the contact load is held constant, since $a \propto (PR)^{1/3}$ (Ref. 38). Another aspect of the radiused electrode is that the pressure distribution at the periphery ($r = a$) of the contact approaches zero $\sigma_n \propto \{1-(r/a)^2\}^{1/2}$, whereas that of the conventional electrode containing a flat weld face approaches infinity $\sigma_n \propto \{1-(r/a)^2\}^{-1/2}$ (Ref. 38). This means that the interface resistance, and hence the heat input, is distributed more toward the periphery for the radiused electrode as compared to the flat-faced conventional electrode. The larger contact radius and redistribution of heat toward the periphery makes the radiused electrode design an ideal candidate to widen the weld

shoulder at the sheet surface, and thereby increase the FGHAZ angle.

Electrode Design DOE

To identify the optimal electrode face diameter (FD) and radius of curvature (FR) that maximize the FGHAZ angle, another simulation-based optimization DOE was performed. The process variables identified using the screening DOE, namely, weld force (HF) and weld time (TW), were also included. The factor levels and other simulation settings for the DOE are presented in Table 4. The main effect and interaction plots for electrode design DOE responses for FGHAZ orientation and weld nugget size are shown in Fig. 7C, D. The FGHAZ angle showed a maximum at an intermediate face diameter of 7 mm. The interaction between hold force (HF) and weld time (TW) are expected as the total heat input into the sheet that governs the size and distribution of weld microstructural zones is a direct function of HT and TW. The radiused electrode with face diameter 7 mm and face radii of curvature 60, 80, and 100 mm were selected for initial trials.

Weld Test Microstructural Results

Spot welds were produced using the electrodes identified from the simulation-based DOE using the optimized single pulse weld schedule obtained from the screening DOE. The process and electrode design parameters are shown in Table 5. The control sample of spot welds was made using the conventional electrode and multipulse weld schedule listed in Table 1. The welds were sectioned and the FGHAZ angle and nugget diameter were measured using the microstructural quantification techniques described previously. For the purpose of comparing the electrode designs, the data are plotted on a map showing FGHAZ angle vs. the nugget diameter. A comparison of representative maps for simulation based DOE and the experimental test welds is shown in Fig. 8A.

Although the FGHAZ angles measured from the modeling study matched better with the validation test results, as shown in Fig. 3, a difference of ~10 deg between predicted and measured maps for the conventional flat-faced electrode and multipulse schedule was observed. This can be attributed to the lower predicted nugget sizes as the model cannot accurately reproduce the weld deformation at the faying interface. In contrast, the maps from simulations and tests for radiused electrode and optimized schedule are in closer agreement, although the model predicts a marginally higher FGHAZ angle.

For a nominal nugget size of 5.5 mm, the welds made using the optimized radiused weld electrode (7-mm FD, 60-mm FR) showed a significant increase in the FGHAZ angle of ~17 deg (23%) as compared to the conventional welding process and electrodes — Fig. 8B, C. This is greater than the ~5-deg increase predicted by modeling results. The dataset obtained from the electrode with an 80-mm radius of curvature showed slightly better results than the 60-mm radius of curvature electrode, which is suggested by the trends observed earlier from Fig. 7C. The optimized electrode and schedule also produced an hourglass-shaped nugget and a narrower FGHAZ. It is expected that this increase in FGHAZ orientation angle and narrower FGHAZ width should significantly improve high cycle fatigue life.

Conclusions

Careful microstructural examination of numerous spot weld fatigue samples of AHSS found that the spatial orientation of the FGHAZ influenced the fatigue performance of the weld, especially high cycle fatigue. The FGHAZ that had high angles relative to the faying interface or were located well beyond the notch root improved fatigue performance due to retarded crack growth rates as a result of either 1) the crack growing at nonpreferred angles with reduced stress intensity and enhanced mixity or 2) the crack deflecting into the weld nugget where it encounters the hard nugget structure. A design of experiment study utilizing finite element simulations was used to optimize both the weld process and electrode design to maximize the orientation angle of the FGHAZ. The optimal electrode design showed a 23% increase in the FGHAZ angle (for a nominal nugget size of 5.5 mm) compared to a conventional weld electrode and multipulse schedule. It is expected that the high cycle fatigue performance of spot welded joints made using the optimal electrode design and weld schedule will be improved, allowing further reduction in material gauge for parts that are limited by their fatigue strength.

Acknowledgments

The authors would like to thank Dr. Wenqi Zhang from SWANTEC, Inc., for initial support and consultation regarding SORPAS® software. Input from GM R&D colleagues is acknowledged with thanks to Dr. Wayne Cai for input on the welding simulations, Dr. Arun Kumar for AHSS materials, and Dr. Sushil Mishra and Shashank Tiwari for microstructure/EBSD data analysis. Lab support from Yelena Myasnikova, Manjunath Kr-

ishnappa, and Krishnamoorthy R is also acknowledged.

References

- Bonnen, J. J. F., Agrawal, H., Amaya, M. A., Iyengar, R. J., Kang, H., Khosrovaneh, A. K., Link, T. M., Shih, H.-C., Walp, M., and Yan, B. 2006. Fatigue of advanced high strength steel spot-welds. *SAE Technical Paper Series* 2006-01-0978.
- Yan, B., Zhu, H., Lalam, S. H., Baczkowski, S., and Coon, T. 2004. Spot weld fatigue of dual phase steels. *SAE Technical Paper Series* 2004-01-0511.
- Sigler, D. R., and Vanimisetti, S. K. 2012. HAZ geometry in advanced high strength steel spot welds and its effect on fatigue performance. *Proceedings AWS Sheet Metal Welding Conference XV*, Livonia, Mich., Oct. 2–5.
- Rossillon, F., Galtier, A., Robert, J. L., Duchet, M., Lens, A., and Oikawa, H. 2008. Effect of welding cycle in the fatigue behavior of resistance spot welded dual phase steels. *Welding in the World* 52(11–12): 30–41.
- Yang, Y. P., Babu, S. S., Orth, F., and Peterson, W. 2008. Integrated computational model to predict mechanical behavior of spot weld. *Sci. Tech. of Welding & Joining* 13(3): 232–239.
- Ma, C., Chen, D. L., Bhole, S. D., Boudreau, G., Lee, A., and Biro, E. 2008. Microstructure and fracture characteristics of spot-welded DP600 steel. *Mat. Sci. & Eng. A* 485: 334–346.
- Long, X., and Khanna, S. K. 2007. Fatigue properties and failure characterization of spot welded high strength steel sheet. *Int. J. Fatigue* 29: 879–886.
- McMahon, J. C., Smith, G. A., and Lawrence, F. V. 1990. Fatigue crack initiation and growth in tensile-shear spot weldments. *ASTM-STP-1058*, pp. 47–77.
- Lawrence, F. V., Wang, P. C., Ho, N.-J., and Corten, H. T. 1983. Estimating the fatigue resistance of tensile-shear spot welds. *UIUC FCP Report No. 48* UILU-ENG-83-3604.
- Milititsky, M., Pakalnins, E., Jiang, C., and Thompson, A. K. 2003. On characteristics of DP600 resistance spot welds. *SAE Tech Paper Series* 2003-01-0520.
- Nakayama, E., Miyahara, M., and Okamura, K. 2004. Prediction of fatigue strength of spot-welded joints based on local material strength properties measured using small specimen. *J. Soc. Mat. Sci., Japan* 53(10): 1136–1142.
- Pan, N., and Sheppard, S. D. 2003. Stress intensity factors in spot welds. *Engineering Fracture Mechanics* 70: 671–684.
- Marya, M., and Gayden, X. Q. 2005. Development of requirements for resistance spot welding dual-phase (DP600) steels Part 1 — The causes of interfacial fracture. *Welding Journal* 84: 172-s to 182-s.
- Kim, B. J., Ryu, S. H., and Lim, B. S. 2004. Fatigue crack growth behavior of heat affected zone in P92 steel weldment. *Metals and Materials International* 10(1): 19–25.
- Tong, W., Tao, H., Jiang, X., Zhang, N., Marya, M. P., Hector, L. G., and Gayden, X. Q. 2005. Deformation and fracture of miniature tensile bars with resistance-spot-weld microstructures. *Metallurgical and Materials Transaction A* 36A: 2651–2669.
- Tao, H., Tong, W., Hector, L. G., and Zavattieri, P. D. 2007. Uniaxial tensile and simple shear behavior of resistance spot-welded dual-phase steel joints. *J. Mat. Engineering and Performance*, ASM International (DOI: 10.1007/s11665-007-9170-8).
- Swantec, Inc. 2009. *SORPAS Enterprise version 10 User Manual*.
- Zhang, W. 2003. Design and implementation of software for resistance welding process simulations. *SAE Technical Paper Series* 2003-01-0978.
- Khan, I., Kuntz, M. L., Zhou, Y., Chan, K., and Scotchmer, N. 2007. Monitoring effect of RSW pulsing on AHSS using FEA (SORPAS) software. *SAE Technical Paper Series* 2007-01-1370.
- Minitab, Inc. 2006. *MINITAB Professional version 15 User Manual*.
- Metallography and microstructures, Vol. 9, 2009. *ASM Materials Information Handbook Online* (<http://products.asminternational.org/hbk/index.jsp>).
- Media Cybernetics, Inc. 2001. *Image-Pro Plus version 5.0 User Manual*.
- Pook, L. P. 1979. Approximate stress intensity factors obtained from simple plate bending theory. *Eng. Fract. Mech.* 12: 505–522.
- Zhang, S. 1999. Approximate stress intensity factors and notch stresses for common spot-welded specimens. *Welding Journal* 78(5): 173-s to 179-s.
- Lin, P.-C., and Pan, J. 2008. Closed-form structural stress and stress intensity factor solutions for spot welds in commonly used specimens. *Eng. Fracture Mechanics* 75: 5187–5206.
- Wang, D.-A., and Pan, J. 2005. A computational study of local stress intensity factor solutions for kinked cracks near spot welds in lap-shear specimens. *Int. J. Solids Structures* 42: 6277–6298.
- Vanimisetti, S. K., and Sigler, D. R. 2013. A computational study of the effect of process-induced weld cracks on fatigue performance of AHSS spot welds. To be submitted to the *Welding Journal*.
- Dassault Systèmes. 2009. *Abaqus version 6.9 Online Documentation*.
- Bhadeshia, H. K. D. H., and Honeycombe, R. W. K. 2006. *Steels: Microstructure and Properties*, 3rd Ed., Butterworth-Heinemann.
- Teplot, Inc. 2008. *Tecplot 360 User's Manual*.
- Radaj, D. 1990. Local fatigue strength characteristic values for spot welded joints. *Engineering Fracture Mechanics* 37(1): 245–250.
- Biner, S. B. 2003. Fatigue crack growth studies under mixed-mode loading. *Int. J. Fatigue* 23: S259–S263.
- Newman, J. A., and Dowling, N. E. 1998. A crack growth approach to life prediction spot-welded lap joints. *Fatigue and Fracture of Engineering Materials & Structures* 21: 1123–1132.
- Guo, Y. H., Srivatsan, T. S., and Padovan, J. 1994. Influence of mixed-mode loading on fatigue-crack propagation. *Engineering Fracture Mechanics* 47(6): 843–866.
- Qian, J., and Fatemi, A. 1996. Fatigue crack growth under mixed-mode I and II loading. *Fatigue Fract. Engng. Mater. Struct.* 19(1): 1277–1284.
- Lin, S.-H., Pan, J., Wing, P., and Chiang, J. 2006. A fatigue crack growth model for spot welds under cyclic loading conditions. *Int. J. Fatigue* 28: 792–803.
- ASM International. 2009. *Fatigue and Fracture, Vol. 19 ASM Materials Information Handbook Online* (<http://products.asminternational.org/hbk/index.jsp>).
- Johnson, K. L. 1985. *Contact Mechanics*. Cambridge University Press.